Supporting Information

Coordination anion effects on the geometry and magnetic interaction of binuclear Dy_2 single-molecule magnets

Jinjiang Wu[a,b], Xiao-Lei Li[a], Léo La Droitte,[c] Olivier Cador,[c] Boris Le Guennic,[c]* and Jinkui Tang[a,b]*

[a]*State Key Laboratory of Rare Earth Resource Utilization, Changchun Institute of Applied Chemistry, Chinese Academy of Sciences, Changchun, 130022, P. R. China.*
[b]*School of Applied Chemistry and Engineering, University of Science and Technology of China, Hefei 230026, P. R. China.*
[c]*Univ Rennes, CNRS, ISCR (Institut des Sciences Chimiques de Rennes) - UMR 6226, F-35000 Rennes, France.*

Corresponding Author:
Boris Le Guennic, *E-mail: boris.leguennic@univ-rennesl.fr*
Jinkui Tang, *E-mail: tang@ciac.ac.cn*

Table S1. Crystallographic data for complexes **1** and **2**.

Compound	**1**	**2**
Formula	$C_{76}H_{74}Dy_2N_{12}O_6S_2$	$C_{74}H_{74}Dy_2N_{12}O_{14}$
Mr	1640.59	1680.45
Temperature/K	173.0	173.0
Crystal system	Triclinic	Monoclinic
Space group	$P\bar{1}$	$P2_1/n$
a/Å	11.6924(4)	14.6039(9)
b/Å	12.8898(4)	15.8167(9)
c/Å	13.8753(4)	16.5425(10)
α/°	96.547(1)	90
β/°	100.241(1)	107.585(2)
γ/°	113.931(1)	90
Volume/Å^3	1840.2(5)	3642.5(4)
Z	1	2
ρcalc/g·cm^{-3}	1.480	1.532
F(000)	826.0	1692.0
Crystal size/mm^3	0.12×0.24×0.25	0.6×0.4×0.2
Reflns collected	20505	74904
R_{int}	0.0563	0.0485
GOF on F^2	1.072	1.151
*R_1, wR_2 [$I >= 2\sigma(I)$]	0.0552, 0.1539	0.0227, 0.0521
*R_1, wR_2 [all data]	0.0597, 0.1595	0.0284, 0.0561
CCDC	2088272	2088273

*R_1 = S||*F*o| − |*F*c||/S|*F*o| for *F*o > 2s(*F*o); wR_2 = (Sw(*F*o^2 − *F*c^2)^2/S(w*F*c^2)^2)$^{1/2}$ all reflections, w =1/[s^2(*F*o^2)+(0.1557P)^2] where P = (*F*o^2+2*F*c^2)/3

Table S2. Selected bond distances (Å), angles (º) for complexes **1** and **2**.

	Compound	
	1	**2**
Dy(1)−O(1)	2.286(3)	2.289(0)
Dy(1)−O(1a)	2.345(1)	2.301(6)
Dy(1)−O(2)	2.187(7)	2.219(6)
Dy(1)−O(3)	2.214(0)	2.212(5)
$Dy(1)-O_{nitrate}$		2.212(5)
		2.668(8)
Dy(1)−N(1)	2.623(0)	2.546(0)
Dy(1)−N(2)	2.529(7)	2.730(7)
$Dy(1)-N_{thiocyanate}$	2.425(6)	
Dy···Dy	3.7441(6)	3.7522(5)
Dy(1)−O(1)−Dy(1a)	107.8(7)	109.6(4)
$Dy-O_{average}$	2.258(0)	2.353(5)
$Dy-N_{average}$	2.525(6)	2.638(0)

Table S3. Lanthanide geometry analysis by SHAPE software for **1** and **2**.

Central atom	Coordination Polyhedron	CShM Values
1 Dy1	Hexagonal pyramid (HPY-7 C_{6v})	18.645
	Pentagonal bipyramid (PBPY-7, D_{5h})	6.918
	Capped octahedron (COC-7, C_{3v})	**0.935**
	Capped trigonal prism (CTPR-7, C_{2v})	1,247
	Johnson pentagonal bipyramid J13 (JPBPY, D_{5h})	9.275
2 Dy1	Hexagonal bipyramid (HBPY-8, D_{6h})	14.052
	Cube (CU-8, Oh)	9.788
	Square antiprism (SAPR-8, D_{4d})	3.368
	Triangular dodecahedron (TDD-8, D_{2d})	**2.752**
	Johnson gyrobifastigium J26 (JGBF-8, D_{2d})	13.062

Table S4. Computed energy levels (the ground state is set at zero), composition of the *g*-tensor (g_x, g_y, g_z) and the main components (>10%) of the wavefunction for each m_j state of the ground-state multiplet $^6H_{15/2}$ of individual Dy^{III} center for **1**.

KD	Energy (cm^{-1})	*g*			Wavefunction
1	0.0	0.0	0.0	19.8	98.1% |±15/2>
2	249.0	0.1	0.1	16.7	92.9% |±13/2>
3	404.8	1.0	1.6	12.6	68.1% |±11/2> + 14.7% |±5/2> + 10.7% |±7/2>
4	461.4	9.2	7.2	2.8	45.1% |±3/2> + 22.4% |±1/2> + 15.1% |±9/2>
5	508.5	2.3	4.4	11.3	26.8% |±7/2> + 19.8% |±9/2> + 19.7% |±1/2> + 14.8% |±11/2> + 14.7% |±5/2>
6	530.3	3.0	5.6	9.1	37.6% |±9/2> + 26.5% |±5/2> + 15.0% |±1/2>
7	566.3	1.5	3.6	12.6	32.7% |±7/2> + 22.7% |±1/2> + 19.4% |±3/2> + 16.5% |±9/2>
8	726.5	0.0	0.0	19.3	31.1% |±5/2> + 25.7% |±3/2> + 20.4% |±7/2> + 16.3% |±1/2>

Table S5. Computed energy levels (the ground state is set at zero), composition of the *g*-tensor (g_x, g_y, g_z) and the main components (> 10%) of the wavefunction for each m_j state of the ground-state multiplet $^6H_{15/2}$ of individual Dy^{III} center for **2**.

KD	Energy (cm^{-1})	*g*			Wavefunction
1	0.0	0.0	0.0	19.7	97.3 ± 15/2>
2	172.5	0.3	0.8	15.0	72.2 ± 13/2>
3	238.1	0.8	1.8	11.1	39.3 ± 11/2> + 19.6 ± 3/2> + 11.8 ± 7/2> + 10.9 ± 1/2>
4	293.4	1.9	4.0	11.0	27.0 ± 9/2> + 19.6 ± 7/2> + 17.0 ± 5/2> + 11.5 ± 1/2> + 10.8 ± 11/2>
5	330.9	2.5	6.2	11.7	30.0 ± 1/2> + 20.2 ± 3/2> + 15.3 ± 5/2> + 14.6 ± 11/2>
6	430.1	0.2	1.2	15.3	20.4 ± 9/2> + 18.6 ± 11/2> + 18.2 ± 3/2> + 12.5 ± 7/2> + 12.5 ± 5/2> + 12.5 ± 1/2>
7	525.6	0.7	1.2	15.4	24.5 ± 1/2> + 24.0 ± 7/2> + 17.9 ± 9/2> + 11.0 ± 5/2> + 10.5 ± 3/2> + 10.3 ± 11/2>
8	558.8	0.4	2.0	17.0	29.5 ± 5/2> + 22.3 ± 3/2> + 20.0 ± 7/2> + 14.1 ± 9/2>

Table S6. Computed exchange energy levels (the ground state is set at zero), composition of the *g*-tensor (g_x, g_y, g_z) and tunnelling splitting value for **1**.

Energy (cm^{-1})		***g***		**Tunneling splitting (cm^{-1})**
0.00	0.0	0.0	39.5	7.6×10^{-9}
0.49	0.0	0.0	0.0	3.31×10^{-8}

Table S7. Computed exchange energy levels (the ground state is set at zero), composition of the *g*-tensor (g_x, g_y, g_z) and tunnelling splitting value for **2**.

Energy (cm^{-1})		***g***		**Tunneling splitting (cm^{-1})**
0.00	0.0	0.0	0.0	2.46×10^{-6}
2.83	0.0	0.0	39.3	4.01×10^{-6}

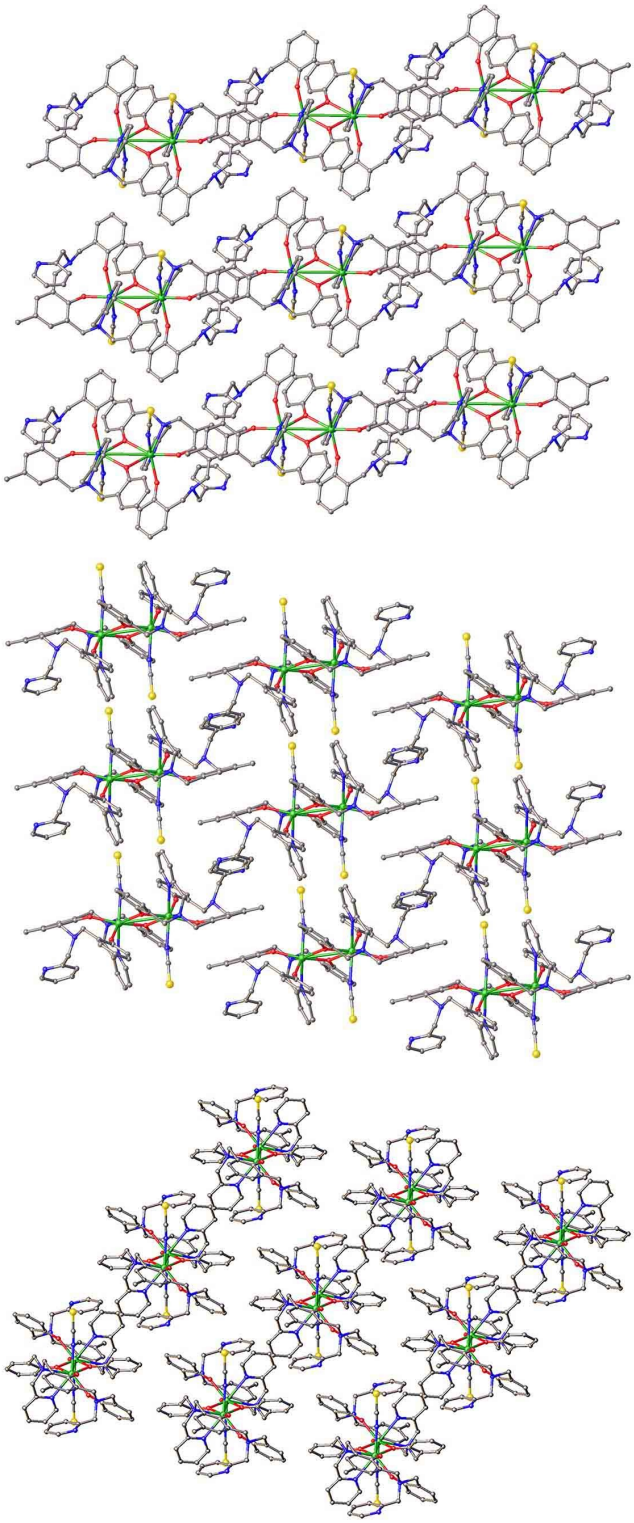

Figure S1. Packing arrangement along the crystallographic *a* (top), *b* (middle) and *c* (bottom) axis for **1**. Color code: purple, Dy; red, O; blue, N; gray, C; yellow, S.

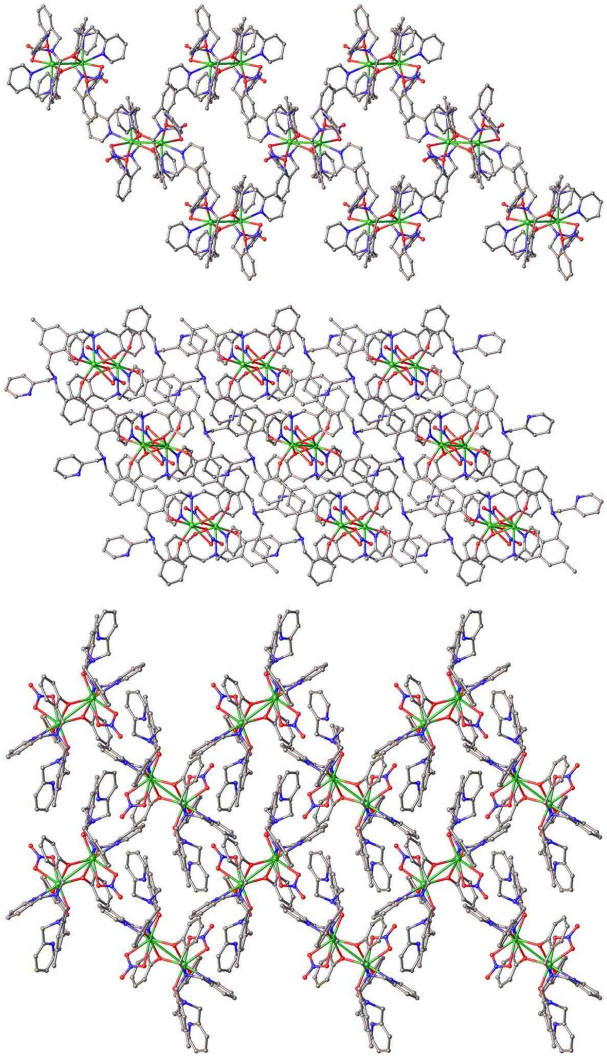

Figure S2. Packing arrangement along the crystallographic a (top), b (middle) and c (bottom) axis for **2**. Color code: purple, Dy; red, O; blue, N; gray, C.

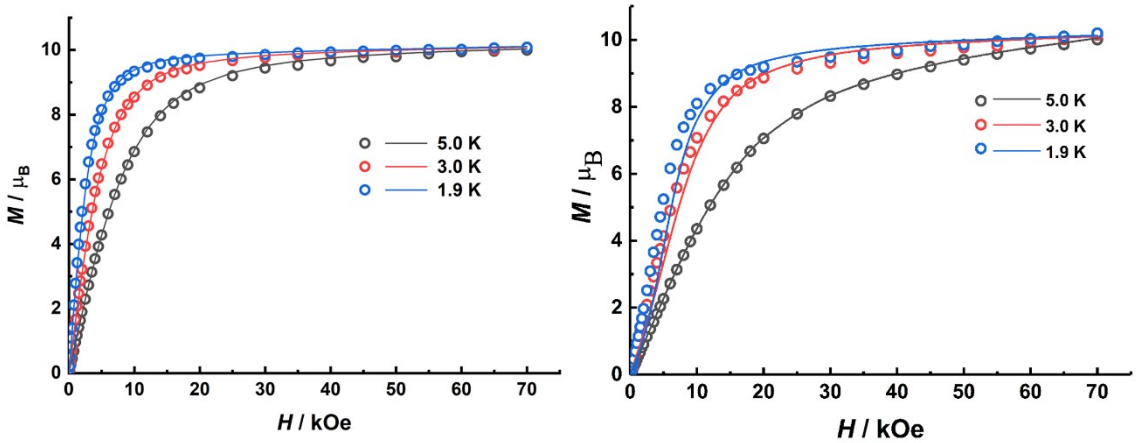

Figure S3. Field dependences of magnetization in the field range 0−70 kOe and at the range of 1.9−5.0 K for **1** (left) and **2** (right). Experimental values as empty dots while calculated curves are represented as full lines.

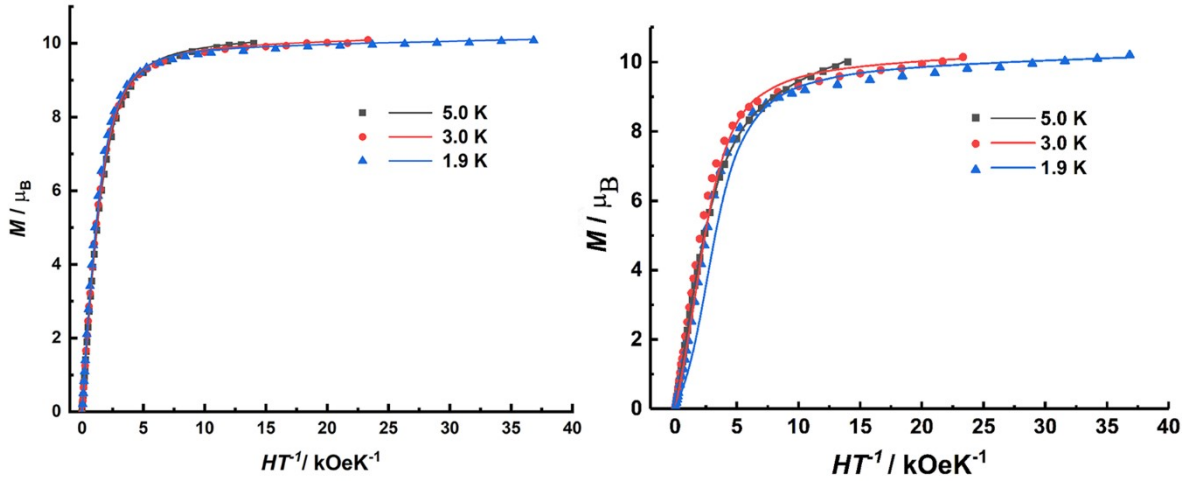

Figure S4. Plots of the reduced magnetization *M versus H*/*T* for **1** (left) and **2** (right). Experimental values as symbols while calculated curves are represented as full lines.

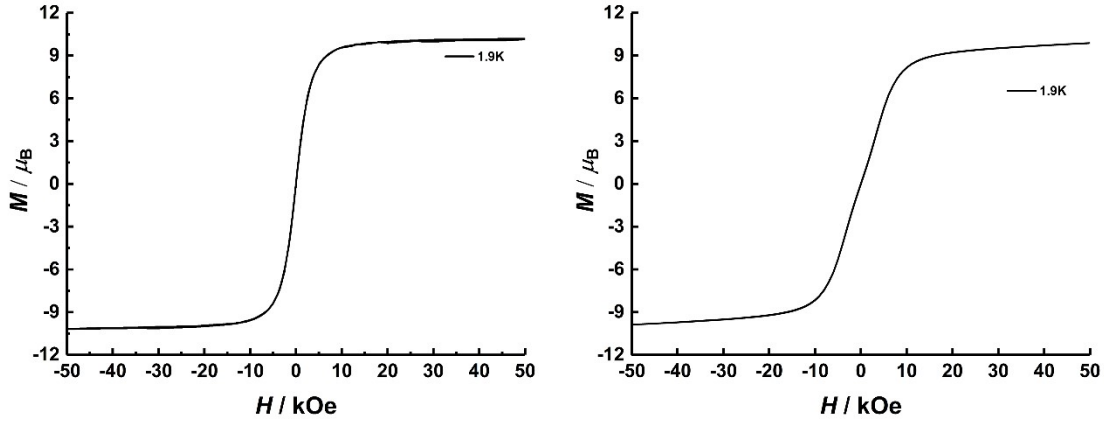

Figure S5. Variable magnetic field magnetization measurement for **1** (left) and **2** (right) at 1.9 K with an averaged sweep rate of 27 Oe/s.

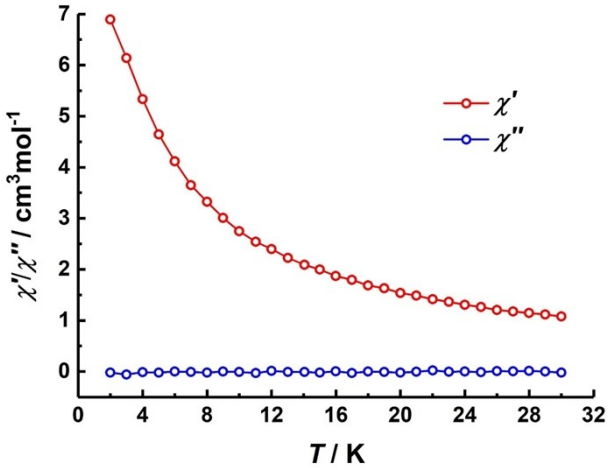

Figure S6. Temperature dependence under zero dc field of the in-phase (red) and the out-of-phase (blue) ac susceptibility component at 997 Hz for **2**.

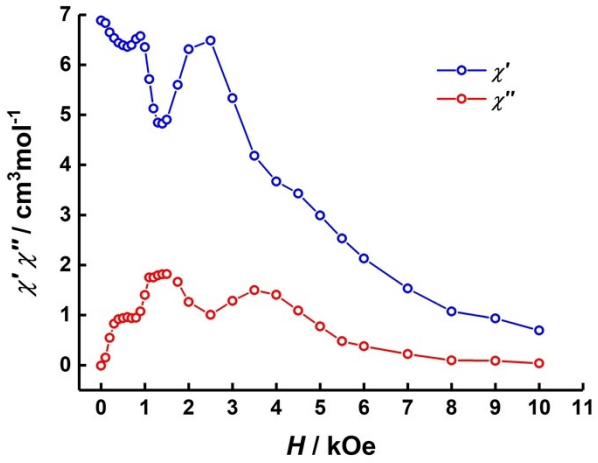

Figure S7. Field dependence of the in-phase (red) and the in-phase (blue) ac susceptibility component at 1.9 K and 997 Hz for **2**.

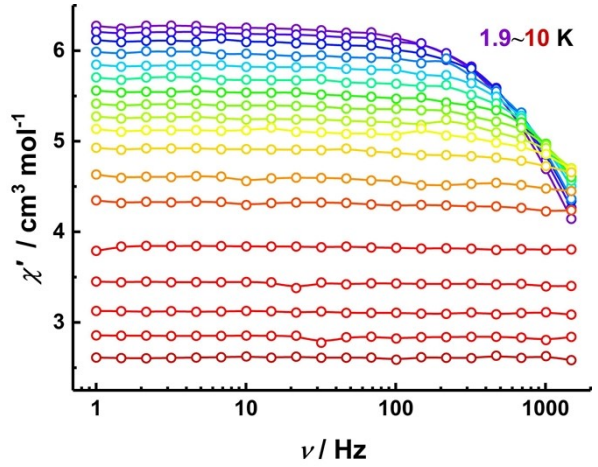

Figure S8. Frequency dependence of the out-of-phase ac susceptibility component under a 1100 Oe applied dc field for **2**.

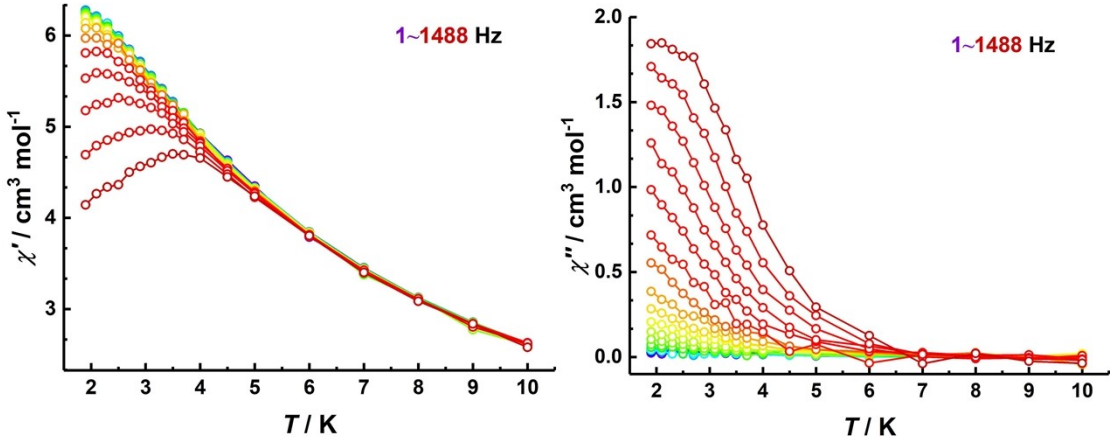

Figure S9. Frequency dependence of the in-phase (left) and out-of-phase (right) ac susceptibility component under a 1100 Oe applied dc field for **2**.

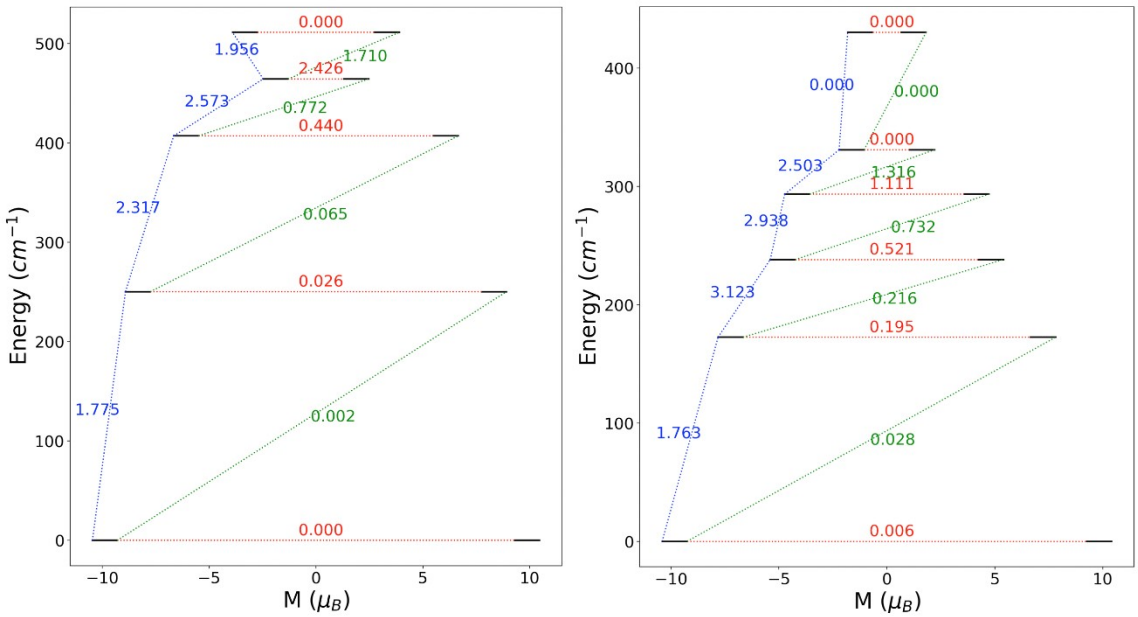

Figure S10. Energies (in cm^{-1}) and projected μ_Z (in μ_B) values along the ground magnetic axis for individual Dy^{III} in complexes **1** (left) and **2** (right). Black lines represent the eight Kramers doublets of individual Dy^{III}. The values of the magnetic (i.e. isotropic Zeeman) transition moments between the states are given for comparison. The values in red correspond to QTM (for the GS) and TA-QTM (for the ESs) mechanisms of the magnetization relaxation, whereas blue and green values correspond to Orbach mechanisms.

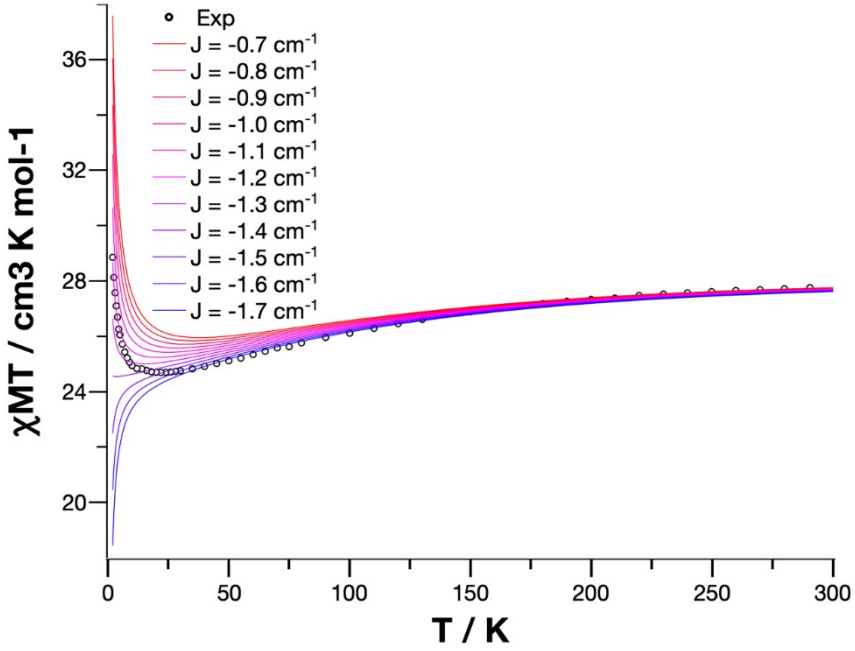

Figure S11. Temperature dependent $\chi_M T$ values for **1** in dots with the calculated curves in full lines for a screening of the J_{exch} value from -0.7 cm^{-1} to -1.7 cm^{-1}.

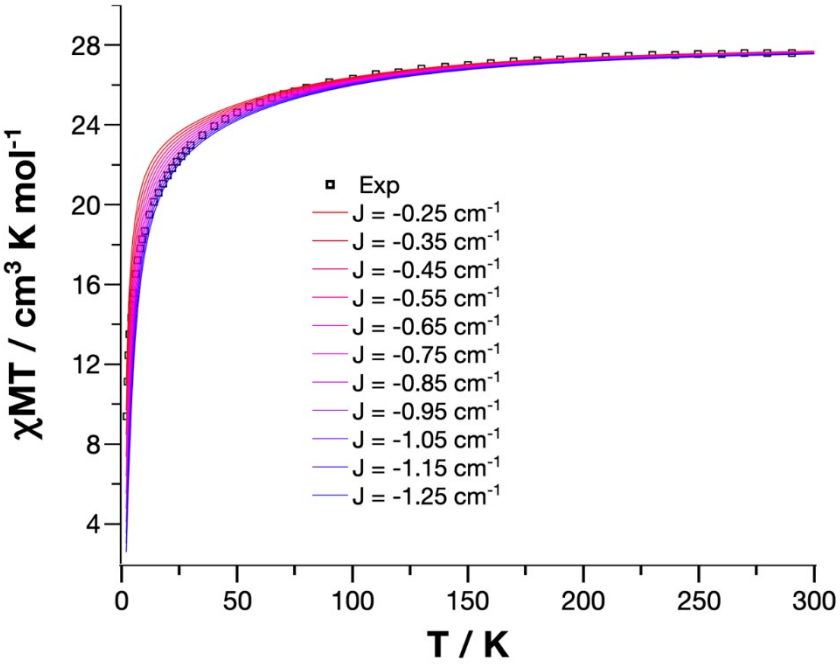

Figure S12. Temperature dependent $\chi_M T$ values for **2** in squares with the calculated curves in full lines for a screening of the J_{exch} value from -0.25 cm^{-1} to -1.25 cm^{-1}.